

# Improved silicon solar cells by tuning angular response to solar trajectory

Received: 2 August 2024

Martin A. Green  & Zibo Zhou

Accepted: 19 December 2024

Published online: 02 January 2025

 Check for updates

Silicon solar cell costs are reducing dramatically with these cells now providing the majority of new electricity generation capacity worldwide. Cost reduction has been via economies of scale and steadily increasing sunlight energy conversion efficiency. The best experimental cells at 27.4% efficiency approach the 29.4% figure almost universally regarded as the limit on silicon cell performance. Here we show that assumptions in deducing this limit are too restrictive, since failing to incorporate sunlight directionality. Furthermore, we show how this directionality and the cell's angular response can be quantified compatibly, using projections of angular dependencies of both onto the solar module plane. Even simple schemes for exploiting directionality, including installing solar modules facing the equator at near-latitude tilt, increase theoretical limiting efficiency above 29.4%. Highest gains are for cells designed for sunlight tracking systems, including common 1-axis trackers, with such cells having theoretical efficiency limits > 30%. In this work, we provide a strategy for ongoing improvements in commercial cell efficiency over this decade, additionally lowering cost via reduced cell thickness.

Recent solar cost reductions<sup>1</sup> have been accompanied by commercialisation of increasingly sophisticated silicon cell technology targeting increased energy conversion efficiency. Although tandem stacks of multiple bandgap cells offer even higher efficiencies, commercialising the leading perovskite-silicon tandem candidate<sup>2</sup> continues to be delayed by perovskite stability challenges. Consequently, further improving silicon cells to extract their full efficiency potential while reducing costs, such as by using thinner cells, will remain critical over this decade.

Following the 1954 announcement of the first 4% efficient silicon cells<sup>3</sup>, efficiency limit calculations soon followed<sup>4,5</sup>, with 21.7% and 20.3% deduced in 1955 and 1956. In a landmark 1961 study<sup>6</sup>, Shockley and Queisser (SQ) derived much higher fundamental limits, determined by cell radiative properties. Although deducing only 26% efficiency for silicon under 6000 K blackbody illumination, their approach gives a much higher 33.3% efficiency under the now-standard Air Mass 1.5 solar reference spectrum. Since silicon's indirect bandgap makes silicon cells radiatively inefficient<sup>7</sup>, relevance of the SQ approach to silicon was largely discounted. In 1984, Green<sup>8</sup> showed that intrinsic Auger recombination, whereby photogenerated carriers

give their energy to neighbours unable to use it effectively, limits silicon cell performance similarly to radiative processes in the SQ approach. He deduced an efficiency limit of 29–30% for cells >100 μm thick, but >30% for cells <100 μm thick.

In a slightly later paper, Tiedje et al.<sup>9</sup> extended Green's analytical approach using computer modelling, placing restrictions on sunlight absorption using Yablonovitch's then recently published light-trapping theory<sup>10</sup>. This showed sunlight randomisation increases the average pathlength of weakly-absorbed light in the cell, the Z factor, by  $4n^2$  where  $n$  is the cell's refractive index, a massive ~50 times boost for silicon. While conclusions were also that limits were 29–30% for cells >100 μm thick<sup>9</sup>, this work predicted peak efficiency around 100 μm thickness, decreasing for thicknesses <100 μm. Subsequent refinements reinforce these conclusions<sup>11–14</sup>, with the presently accepted 29.4% limiting efficiency first reported<sup>11</sup> in 2013, reaffirmed<sup>12</sup> in 2022.

This difference from Green's earlier conclusions, arising from different absorption assumptions (Fig. 1a, b), becomes important as commercial cells approach 100-μm thickness<sup>15</sup>. Green<sup>8</sup> assumed all incoming light was absorbed, only strictly possible if collimated and hence having zero entropy, consistent with calculating upper limits.

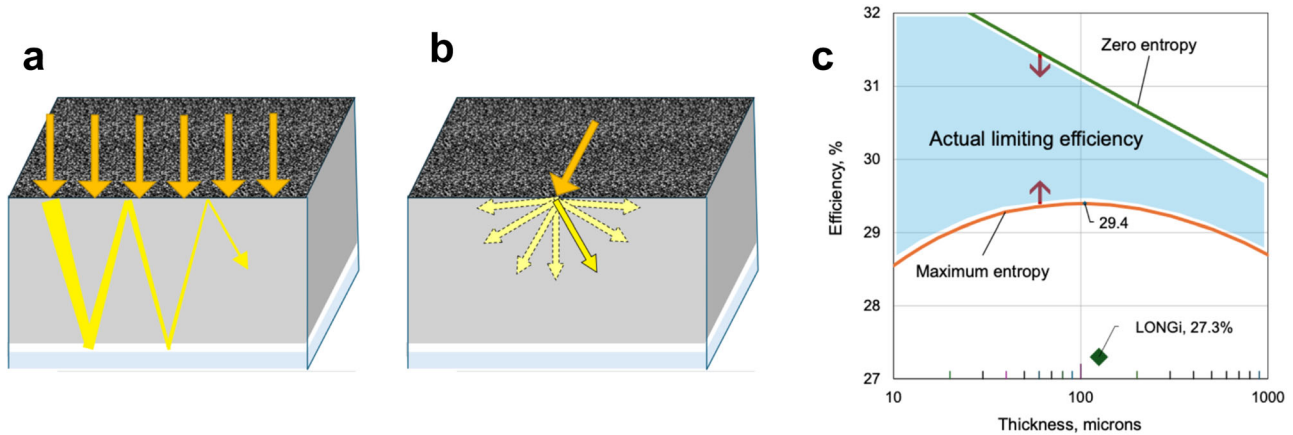


**Fig. 1 | Light absorption assumptions and impact on limiting conversion efficiency.** **a** Green's assumption that light remains trapped until absorbed<sup>8</sup>, possible if light is well collimated, a zero entropy assumption consistent with calculating upper limits. **b** Yablonovitch's assumption<sup>10</sup> that light direction is randomised on entering the cell, effectively assigning it maximum possible entropy, consistent

with finding lower performance bounds. **c** Upper and lower bounds on limiting efficiency for the extreme cases of Fig. 1 (a, b). The 29.4% value previously regarded as a limit<sup>11,12</sup> is seen to be a lower bound, possible to exceed if cells exploit sunlight directionality.

However, Yablonovitch's theory<sup>10</sup> requires complete light randomisation, effectively assigning it maximum possible entropy. Although previously overlooked<sup>11–14</sup>, this produces a lower rather than upper bound on limiting efficiency. Figure 1c compares the two cases, showing the latest calculation using Yablonovitch's approach giving the accepted 29.4% efficiency limit<sup>12</sup>, as well as a zero entropy calculation using identical parameters (Methods).

Since most practical solar systems exploit sunlight directionality, the actual efficiency limit must lie somewhere between the two extremes of Fig. 1c, depending upon the degree of exploitation. The inescapable conclusion is that the cell efficiency bound in any actual system is higher than the presently accepted 29.4% limit. In this work, we show how directionality and the cell's angular response can be quantified compatibly, with practical implications for how cell design must evolve as cell performance pushes closer towards its limits, particularly as cell thickness reduces below 100  $\mu\text{m}$ .

## Results

### Quantifying Directionality

Given daily and seasonal variations and scattering over the terrestrial hemisphere, quantifying sunlight directionality would appear difficult. However, the work of Ivanov and Gueymard<sup>16</sup> alerted us to this possibility. These authors first project accumulated annual radiance onto the terrestrial hemisphere (Fig. 2a) followed by a parallel “fish-eye” projection onto a plane of interest (Fig. 2b). This converts radiance into an irradiance contribution from the same direction on this plane. Figure 2a shows cumulative radiance for Sofia, Bulgaria projected onto the terrestrial hemisphere<sup>16</sup>, with Fig. 2c showing the resulting projection onto a unit circle parallel to the horizontal. However, Fig. 2d shows a more interesting projection onto a unit circle parallel to a south-facing plane, tilted at the latitude angle from horizontal, the well-known “rule-of-thumb” for maximising annual fixed-tilt solar system output<sup>17,18</sup>.

The simplicity of Fig. 2d, with direct sunlight confined to a central band of incident angles, and its worldwide universality alerted us to prospects for quantifying sunlight directionality this way, reinforced by our earlier work exploring approaches for exceeding Yablonovitch's  $4n^2$  enhancement limit using geometrical (non-randomising) schemes<sup>19,20</sup>.

Campbell and Green<sup>19</sup> first showed the  $Z$  limit increased to  $4n^2/\sin^2\theta$  when cells only needed to respond to light within an angle  $\theta$  of the cell normal, such as in sunlight focussing systems.

They then showed<sup>20</sup> that, for some schemes,  $Z$  could exceed  $4n^2$  at some angles at the expense of performance at other angles. This trade-off was subsequently quantified by Yu and Fan<sup>21</sup>, generalising Yablonovitch's result<sup>10</sup> to:

$$\int_0^{\pi/2} d\theta \int_0^{2\pi} Z(\theta, \phi) \cos(\theta) \sin(\theta) d\phi \leq 4\pi n^2 \quad (1)$$

where  $\theta$  and  $\phi$  are altitudinal and azimuthal angles.

Equation (1) has a simple geometric interpretation. If  $Z(\theta, \phi)$  is plotted as for radiance in Fig. 2a, referenced to the cell normal, and the same fish-eye projection used, the average value over the unit circle must be  $\leq 4n^2$ . (In Methods, we extend Eq. 1 to bifacial cells responding to both front and rear light, increasing limits on the  $d\theta$  integral—“ $0-\pi/2$ ” becoming “ $0-\pi$ ”—effectively halving average  $Z$ . However, equal sharing of  $Z$  between front and rear is not mandated, potentially important for cell design).

### Fixed tilt systems and sunlight directionality

Cell design can be optimised for specific applications by selecting light-trapping schemes angularly matched to the input sunlight distribution. As an example, Fig. 2e shows idealised light-trapping projections conforming to Eq. 1 for south-facing modules (northern hemisphere) both at latitude and arbitrary tilt. For latitude tilt, strongest light-trapping is required for the central band representing directions of both direct and strongest diffuse sunlight. If we incorporate a  $2.9^\circ$  half-angle region encircling the solar disc accounting for both circumsolar radiation and alignment accuracy (as for the AM1.5 direct reference spectrum<sup>22</sup>), this band occupies 54.7% of the projected area. Regions outside this band are less critical—associated irradiance is much weaker and blue-rich as shown in Fig. 3, giving proportionately smaller infrared light-trapping gain. Consequently, if modest  $n^2$  boost is assigned to these regions,  $6.5n^2$  is available from the all-important central band while satisfying Eq. (1). This increases limiting efficiency for all cell thicknesses, peaking at 29.7% for cells  $\sim 60 \mu\text{m}$  thick, in the blue zone of Fig. 1c. With cells  $<100 \mu\text{m}$  thick already contemplated to reduce wafer costs<sup>15</sup>, appreciably thinner cells are feasible while improving efficiency.

The “rule-of-thumb” tilt does not necessarily maximise annual energy production<sup>17,18</sup>, generally peaking at lower tilts pointing modules more towards the summer solstice (Fig. 2a, d). This causes the central band projection to droop, as for a horizontal module (Fig. 2c).

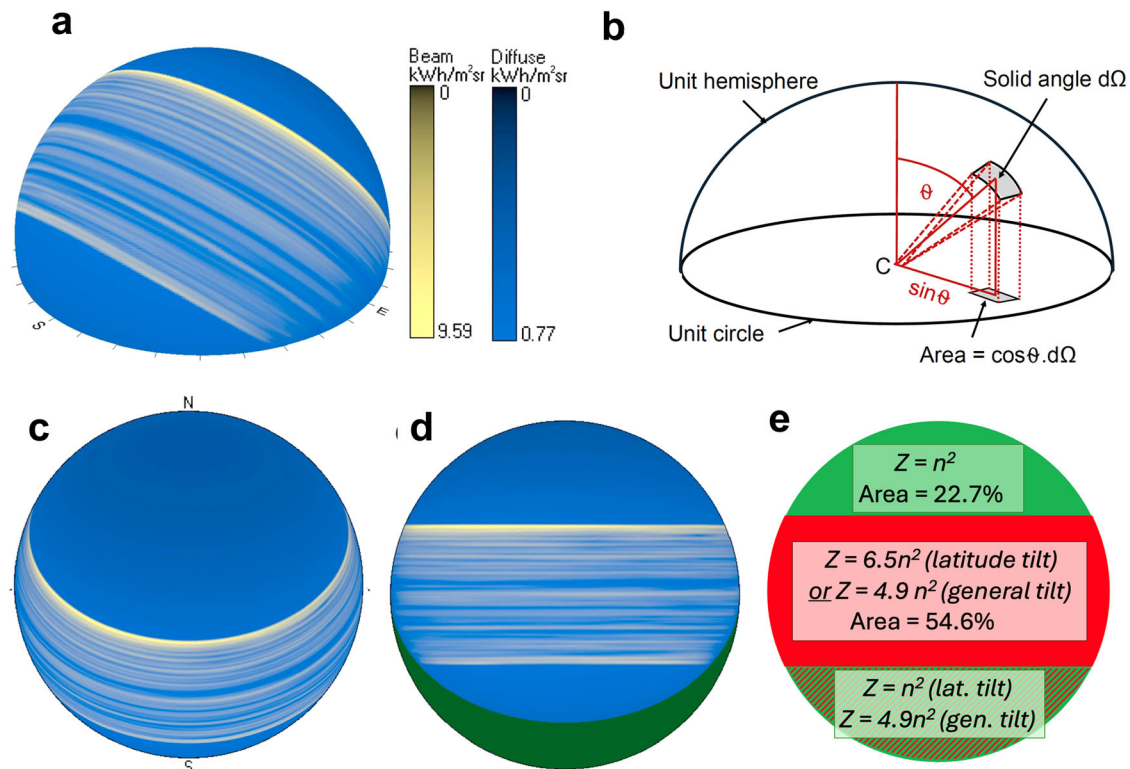


**Fig. 2 | Quantifying sunlight directionality and cell angular response.**  
**a** Accumulated radiance (typical meteorological year) projected onto the terrestrial hemisphere for Sofia (latitude 42.7°N), with different scales for direct and diffuse radiation (in kWh/m<sup>2</sup>/sr)<sup>16</sup>. **b** “Orthographic fisheye” projection from unit hemisphere to unit circle, with the circle plane orientated to match solar module orientation. **c** Projection of Fig. 2a onto a horizontal unit circle<sup>16</sup>. **d** Projection of Fig. 2a onto a unit circle tilted at the latitude angle facing south<sup>16</sup> (lower green region represents ground-reflection). **e** If the pathlength enhancement factor as a function of altitudinal and

azimuthal co-ordinates referenced to the cell normal,  $Z(\theta, \phi)$ , is projected onto the unit hemisphere, then onto the unit circle corresponding to the cell plane, the average value over the circle must be  $\leq 4 n^2$ . Two conforming light-trapping designs shown, one for latitude tilt giving  $6.5 n^2$  enhancement over the central band (where both direct and diffuse light are strongest), with a lower value of  $n^2$  over segments receiving only diffuse light. The second conservatively accommodates arbitrary tilt (including vertical or horizontal orientation), with the central enhancement extended into either lower or upper zones.

All possible tilts are conservatively accommodated by assigning the lower region of Fig. 2e the same  $Z$  as the central band, reducing it to  $4.9 n^2$  over the extended region. This gives limiting efficiency of 29.5–29.6% (vertical deviations accommodated by 180° rotation of cells or modules).

Another growing stationary mounting<sup>23</sup> is vertically installed bifacial modules facing due east and west. Again, direct sunlight projections lie in a band, rotated from horizontal by the complement of the latitude<sup>16</sup>.

### 2-axis trackers

Although 2-axis trackers represent a negligible fraction (<1%) of solar systems installed<sup>24</sup> in 2024, these provide maximum potential for boosting cell efficiency. Ideally, 2-axis trackers align the module normal directly with the sun<sup>25</sup>, projecting it to the centre of the unit circle (Fig. 4a), occupying only  $\sim 1/400$ th of its area even with the  $2.9^\circ$  circumsolar region included.

High  $Z$  consequently can be assigned to the central region without significantly reducing  $Z$  for non-perpendicular light, sufficiently high for cells to approach the zero entropy efficiency limit of Fig. 1c. Assigning  $3 n^2$  to peripheral regions allows  $>390 n^2$  to be assigned to the central region, giving cell limits over 31% for cells  $<100 \mu\text{m}$  thick. The challenge is to find practical schemes sufficiently resonant to attain such high  $Z$  experimentally. The minor  $Z$  reduction for non-normal incidence means cells can perform with limiting efficiency above 29% for non-normal direct sunlight, such as the module receives when backtracking (to avoid shading adjacent trackers at low sun angles).

### 1-Axis Trackers

1-axis trackers are expected<sup>24</sup> to account for  $\sim 60\%$  of large solar power plant installed in 2024 (remainder mostly stationary, fixed-tilt systems). Ideally, these ensure the module normal lies in the plane of the tracker axis and the sun’s direction<sup>25</sup>. The vast majority have NS-axis orientation, being particularly effective<sup>26</sup> at latitudes  $<40^\circ$ . The projected sun-path for less common EW-axis trackers is simpler (Fig. 4b). The sun merely follows a horizontal EW path (not reaching EW boundaries in winter), occupying  $<1/15$ th of the total projected area, again allowing high  $Z$  across this band without significantly sacrificing  $Z$  for incidence outside it. Assigning  $3 n^2$  for the latter allows values  $\sim 19 n^2$  in the band, giving limiting efficiency  $>30\%$  for appropriately designed cells.

The path for more common NS-axis orientation is latitude dependent as shown for  $40^\circ$  latitude (Fig. 4c), generally the highest appropriate for such NS-axis trackers<sup>26</sup>. The path is bounded by sun positions in the morning and evening of the summer solstice and at winter solstice noon, equal to  $\sin(\delta)/\cos(\phi)$  and  $\sin(\delta + \phi)$  times the radius along the axis, respectively. This limits the band area to  $<1/23$ rd of the unit circle (latitudes  $<40^\circ$ ), allowing even better light-trapping trade-offs than for EW-axis trackers.

The case of ideal backtracking for a NS-axis tracker is shown in Fig. 4d. Trackers start close to horizontal in the morning to prevent shading those more westerly. As solar elevation increases, trackers tilt towards the vertical, working towards their optimal orientation (sun in plane of axis and module normal). This is reached when the tracker is at maximum tilt (normally  $60^\circ$  from horizontal), if system is fully

optimised for ground-coverage ratio (module area divided by land area). Rather than 2-region partitioning (Fig. 2e), one could imagine 3-region partitioning, for example, assigning  $4n^2$  for backtracking angles, reduced  $Z$  in diffuse light areas and correspondingly increased  $Z$  in the now reduced areas where optimal tracking occurs.

### Light-trapping structures

Several light-trapping approaches suited for mainstream silicon cells have been previously proposed and analysed<sup>19–21,27–31</sup>, although seldom in the context of linking to the likely angular sunlight distribution in any given application as now possible. The following sections discuss a selection of these, including experimental aspects where available.

### Angular absorption cutoff

The first of such light-trapping approaches was suggested some time ago<sup>19</sup> but takes advantage of the shift of bandpass antireflection coating cutoff to shorter wavelength for obliquely incident light, with the basic concept shown in Fig. 5a. While the cell illustrated accepts near-perpendicular light at all desired wavelengths, obliquely incident light is reflected at infrared wavelengths near the coating cutoff. A concrete example is shown in Fig. 5b.

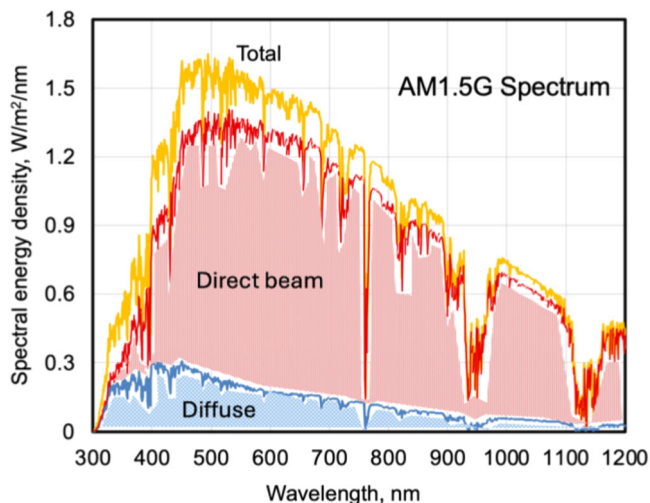


**Fig. 3 | Standard AM1.5 global reference spectrum<sup>22</sup> deconvoluted into direct beam and diffuse components.** The weaker diffuse component is blue-rich with infrared radiation in the 950–1200 nm range benefiting correspondingly less from light-trapping.

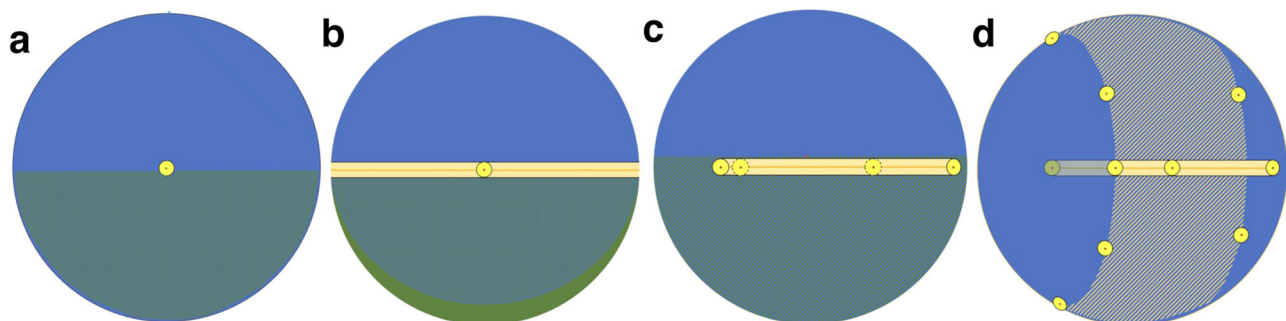


**Fig. 4 | Projected irradiance onto the unit circle for sunlight tracking systems.** **a** Ideal 2-axis tracker confining direct and  $2.9^\circ$  circumsolar radiation to the unit circle centre. **b** Ideal 1-axis tracker on EW-axis, with a simple direct and circumsolar irradiance pattern moving E to W across the unit circle. **c** More common 1-axis tracker on NS-axis, with projected sun-paths latitude dependent, moving N to S

Exploring the angular performance of a 51-layer AR coating shown in Fig. 5b, well-behaved performance prevails up to  $-50^\circ$  from normal. While 1100 nm wavelength light will be strongly coupled in if incident within  $20^\circ$  of the normal, it will be inhibited from being coupled out if scattered into other angles. Above  $60^\circ$ , visible wavelength reflection remains lower than from uncoated glass, but the increasing cut-off shift nonetheless disadvantageously reduces current generation to below that of uncoated glass. This effect already occurs to a minor extent with present glass antireflection coatings but may increase in importance as these become more sophisticated.

### Cross-groove texture

Figure 6a shows cross-grooves<sup>32</sup>, early demonstrated<sup>20</sup> to give  $Z > 4n^2$ . Grooves can be formed using similar etching to present commercial random pyramidal texturing approaches, although complicated by requiring groove location definition. Groove sidewall angles can be controlled within the  $-49$ – $54^\circ$  range ( $-$ intersecting  $\{111\}$  planes), with this angle and slat height to cell thickness ratio important in determining performance (Fig. 1, Supplementary Information).

Figure 6b shows good general-purpose response from a  $49^\circ$  slat design suitable for fixed-tilt and 1- and 2-axis trackers. For near-perpendicular light, limiting efficiency is  $>30\%$  for cells  $<100 \mu\text{m}$  thick, peaking at 30.1% for cells only  $40$ – $50 \mu\text{m}$  thick (Fig. 6c), interesting for 2-axis trackers. The central band in Fig. 6b with average  $Z > 4n^2$  indicates improved performance for modules mounted near-latitude tilt, with bright yellow regions along the horizontal axis boosting 1-axis tracker performance. The montages in Supplementary Figs. 1, 2 indicates the range of light-trapping performance for simple symmetrical grooves.

Some convincing experimental work supporting the strong potential of the cross-grooved approach was reported<sup>33</sup> not long after the “beyond Lambertian” light trapping properties of perpendicular grooves had first been simulated<sup>20</sup>. Experimental absorption properties of bare wafers with different texture combinations on front and rear were reported with cross-grooves showing appreciably stronger long wavelength absorption compared to randomly textured surfaces both sides and textured top, planar rear geometries. The advantage for perpendicular light was shown to be equivalent to an extra  $1 \text{ mA/cm}^2$  increase in current output for a 150 micron thick cell compared to the “both sides textured” case.

### Wavelength-scale texture

2-D gratings (Fig. 7a) using wavelength-scale features provide another light-trapping approach<sup>34</sup>. Perpendicular light boosts reaching  $4\pi n^2$  are calculated using square matrix layout, increasing to  $8\pi n^2/\sqrt{3}$  for hexagonal<sup>34</sup>. Unlike cross-grooves, boosts are very wavelength and

across the module and back (northern hemisphere), shown both for  $40^\circ$  latitude and at the equator (dashed sun positions, giving smallest sun-path). **d** 1-axis tracker on NS-axis (latitude  $40^\circ$ ) with backtracking<sup>25</sup> to prevent adjacent module shading. Modules start the morning horizontal, tilting towards their ideal tracking position as the sun’s altitude increases, then back towards horizontal in the evening.

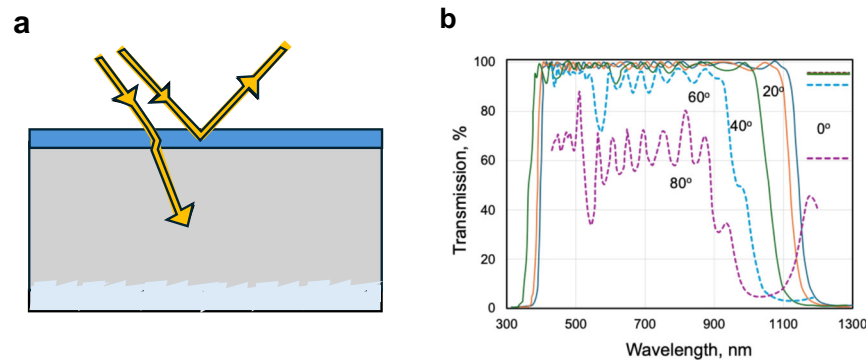


**Fig. 5 | Light-trapping via angular absorption cutoff.** **a** Obliquely incident light is absorbed for a range of angles but reflected once too oblique, correspondingly restricting light escape<sup>19</sup>. **b** Angular response of a 51-layer bandpass antireflection coating designed for space solar cell cover-glass<sup>46</sup>. Of interest is the long-

wavelength absorption edge shift to shorter wavelengths as the incidence angle increases. Also shown (dashed bars to the right) is the transmission through a bare glass surface as a benchmark.

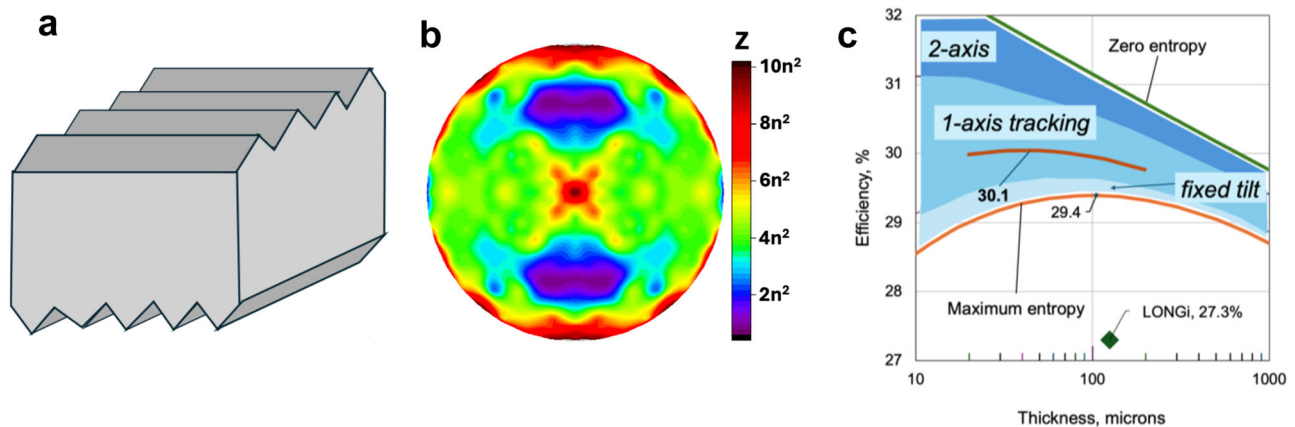


**Fig. 6 | Cross-groove light-trapping scheme and light-trapping performance.** **a** Cross-groove light-trapping<sup>32</sup>, skewing light from escape cones. **b** Unit circle projection of general-purpose cross-groove design (49° groove wall angle).

**c** Limiting efficiency for near-perpendicular light for the specific design of Fig. 6b (line labelled 30.1), also showing approximate boundaries for different applications.

angularly dependent. Averaging results over the wavelength range of interest (Fig. 7b) removes this difficulty, again indicating good general purpose response.

A series of recent papers<sup>35–37</sup> report exceptionally high performance from periodically textured device simulations, exceeding above theoretical bounds.  $Z$  factors over 100,000 are involved, resulting in simulated efficiencies also over 30%. These unphysical results have been traced to premature termination of the finite difference time domain (FDTD) simulation approach used, resulting in temporarily trapped light being treated as absorbed.

### Bifacial cells

An additional cross-groove feature is suitability for bifacial cells, representing >90% of present cell production<sup>24</sup>. These are used either in monofacial modules, largely on rooftops, with detached rear reflectors included in cell encapsulation, or increasingly in transparent-backsheet bifacial modules for field installation, accounting for expected 63% module market share<sup>24</sup> in 2024.

Since light can escape from 2 surfaces, bifaciality halves the  $4n^2$  light-trapping average value, reducing the conventionally calculated limiting efficiency bound to 29.0%, reached with slightly thicker cells (130–170  $\mu\text{m}$  thick). This highlights the future importance of matching cell angular response to sunlight directionality to maintain high efficiency while reducing cell thickness to <100  $\mu\text{m}$ .

With standard cross-grooves, symmetry dictates identical angular response on both surfaces (rotated 90°) hence projected area averages

are  $\leq 2n^2$  on each. With less symmetric structures, say with different groove angles or spacing on each side (Supplementary Information Fig. 2), the more important front-side  $Z$  can be boosted at the expense of the rear-side.

## Discussion

We show that, to reach limiting performance, cells must exploit sunlight directionality in their targeted application. Present power plant applications are divided roughly 40%–60% between fixed-tilt and 1-axis tracking<sup>24</sup>, with different cell designs likely ideal for each, rather than merely different module designs as presently common. Due to increased module orientation control, 1-axis tracking provides higher potential boost, also allowing use of thinner cells. The 29.4% efficiency long regarded as limiting, requiring cells at least 100- $\mu\text{m}$  thick, is increased to 30.1% for cells 60- $\mu\text{m}$  thick or thinner, designed for these trackers. To realise such efficiency, past trends to increasingly sophisticated cell structures must be continued by implementing improved light-trapping. This ensures high thin-cell current, with “state-of-art” surface passivation already producing voltage increase for such cells<sup>15</sup>, crucial to their projected efficiency advantage.

## Methods

### Limiting efficiency calculations

The “maximum entropy” limiting efficiency curves of Figs. 1c, 6c duplicate the published results of Niewelt et al.<sup>12</sup> for intrinsic, undoped silicon cells. The “zero entropy” curves use the same material

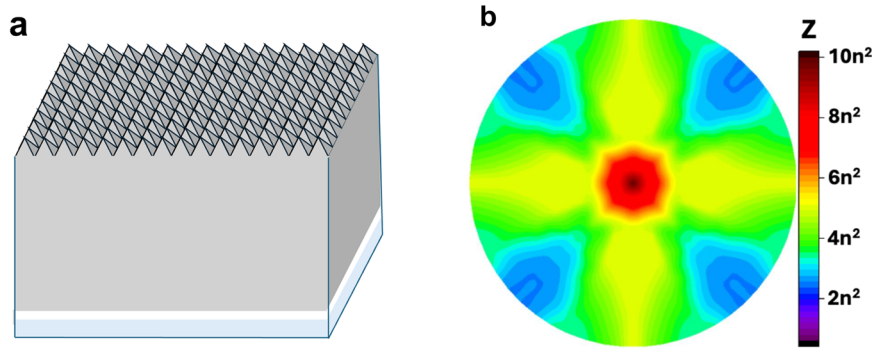


**Fig. 7 | Wavelength-scale light-trapping schemes and light-trapping performance.** **a** 2-D grating with wavelength-scale features<sup>34</sup>. **b** Unit circle projection of ideal grating light-trapping averaged over 950–1200 nm wavelengths (grating period 950 nm).

parameters as in Niewelt et al.<sup>12</sup> and are derived by calculating current-density voltage (J-V) curves near the cell maximum power point for each thickness. First, an electron-hole (np) product is assumed, modelled as uniform throughout the cell, allowing the corresponding cell terminal voltage  $V$  to be calculated using the bandgap narrowing theory of Schenk<sup>38</sup> as implemented in a PV Lighthouse calculator (<https://www.pvlighthouse.com.au/bandgap>). For the relatively low values of  $n$  and  $p$  involved, negligible difference was found using these values and Schenk’s subsequently refined theory<sup>39</sup>.

The photogenerated current density,  $J_{gen}$ , is calculated at  $V$  from the photon fraction absorbed in band-to-band absorption, with most absorbed by free-carrier absorption at high voltages and long wavelengths. From  $J_{gen}$  must be subtracted recombination currents due to Auger and radiative recombination in this limiting efficiency case. Auger recombination was calculated as in the work of Green<sup>8</sup>, considering the reducing Auger recombination coefficients as carrier concentrations increase. For this zero entropy case, radiative recombination is minimised if only a minimal amount is emitted by the cell as given by Eq.4.45 of Green<sup>40</sup>, leaving only a component of radiative recombination due to imperfect photon recycling. Note that this formulation already includes the effective reduction of radiative recombination at high carrier injection levels as noted by Fell et al.<sup>41</sup>.

For other calculations of cell performance when light-trapping values differed from  $4n^2$ , two different approaches were used depending upon the level of detailed knowledge of the light-trapping scheme. Equation (1) of the text gives information on the allowed light-trapping values in the limit of weak absorption, with pathlength enhancement values of  $4fn^2$  allowed at different angles, with  $f$  values above and below unity feasible. To provide an estimate of performance for different  $f$  values, a “quasi-Lambertian” approach was used. Rather than allowing escape of  $1/n^2$  of the remaining light at each surface interaction, as for the Lambertian case<sup>42</sup>, a value of  $1/(fn^2)$  was assigned, giving the correct value in the weak absorption limit while allowing the standard Lambertian calculational procedure to be used. For cases where a specific rather than generic light-trapping scheme is analysed such for the cross-groove calculation of Fig. 6c, the full pathlength distribution function<sup>27,28</sup> is first calculated and the cell output then calculated from this.

### Bifacial cells

Light-trapping limits for both monofacial and bifacial cells can be derived more simply than in earlier work<sup>21</sup> by combining the reciprocal relationship identified by Rau<sup>43</sup> between light emission from a cell and its external quantum efficiency (EQE) with the van Roosbroeck-Shockley equation<sup>44</sup>. We can define the positionally and angularly weighted value of an external cell property  $F(r_s, \theta, \phi, E)$  that, as for EQE, will generally be a function of surface position,  $r_s$ , on surface  $S$ , altitudinal and azimuthal angular coordinates  $\theta$  and  $\phi$  relative to the

surface normal, and photon energy,  $E$ , as:

$$\overline{F(r_s, \theta, \phi, E)} = \frac{\int dS \int_0^{\pi/2} d\theta \int_0^{2\pi} d\phi F(r_s, \theta, \phi, E) \sin\theta \cos\theta d\phi}{\int dS \int_0^{\pi/2} d\theta \int_0^{2\pi} \sin\theta \cos\theta d\phi} \quad (M1)$$

Rau’s relationship<sup>43</sup> for the photon emission rate/unit area from the cell becomes:

$$\text{Photon emission rate/unit area} = \frac{2\pi}{h^3 c^2} \int_0^\infty \frac{(\overline{EQE}_f + \overline{EQE}_r) E^2}{\exp[(E - qV)/kT] - 1} dE \quad (M2)$$

where  $\overline{EQE}_f$  and  $\overline{EQE}_r$  are the above area and angularly weighted EQE for front and rear surfaces, respectively. At each energy, this rate cannot be higher than the photon generation rate within the cell given by van Roosbroeck-Shockley equation<sup>44</sup>.

$$\text{Photon generation rate/unit area} = \frac{2\pi}{h^3 c^2} \int_0^\infty \frac{(4n^2 \alpha W) E^2}{\exp[(E - qV)/kT] - 1} dE \quad (M3)$$

It follows that, for all photon energies,  $\overline{EQE}_f + \overline{EQE}_r \leq 4n^2 \alpha W$ . In the weak absorption limit, in the absence of parasitic absorption, EQE equals the cell absorptance in ideal cases allowing it to be expressed in terms of the pathlength enhancement factor in this limit giving, for example,  $\overline{EQE}_f = \bar{Z}_f \alpha W$ , and the final result:

$$\bar{Z}_f + \bar{Z}_r \leq 4n^2 \quad (M4)$$

For a monofacial cell, an ideal rear reflector corresponds to  $\bar{Z}_r = 0$ , giving a slightly more generalised version of Eq. (1). For a bifacial cell with a symmetrical light-trapping scheme, such as implied by the cross-grooved scheme of Fig. 6a,  $\bar{Z}_f = \bar{Z}_r \leq 2n^2$ . An interesting and potentially important result from the above derivation is that an asymmetrical scheme need not conform to this constraint, meaning schemes where  $\bar{Z}_f > 2n^2$  are possible, if  $\bar{Z}_r < 2n^2$ . This means that the light-trapping performance for light incident on the all-important front of the cell can be boosted at the expense of the response of the less critical rear.

### Ray-tracing simulations

We used the commercial software COMSOL Multiphysics with the Ray Optics module to solve the light propagation within a silicon cell given a specific surface texturing scheme. The geometric optics approach accounts for the reflection and refraction of light rays, assuming the texturing feature size is much larger than the wavelength [COMSOL Multiphysics Reference Manual, 6.1]. We simulated refractive index<sup>45</sup> of 3.51 corresponding to monochromatic light at circa 1200 nm with an artificially low absorption coefficient to model the weak absorption

case. Around 1100 rays were released above the texturing feature covering several unit cells. The initial direction of travel of rays was adjusted to assess the texturing scheme's pathlength enhancement at different incident angles. Effectively, we sampled 1100 different random locations and presented a position-averaged result for a given texturing design. The results remain essentially unchanged on further increasing the number of initially released rays. Due to geometrical symmetry, only a fraction of the azimuth angle range generally needs simulation with the polar angle swept from 0° (normal to surface) to 89°. The silicon cell absorption at different incident angles is compared to that of the single path length, yielding the pathlength enhancement factor  $Z$ . The pathlength distribution function is also calculated and used in calculations of cell current output for the different schemes.

## Data availability

Source data are provided as a Source Data file. Additional data are available from the corresponding author upon request. Source data are provided with this paper.

## References

- Haegel, N. M. et al. Photovoltaics at multi-terawatt scale: waiting is not an option. *Science* **380**, 39–42 (2023).
- Peplow, M. A new type of solar cell is coming. *Nature* **623**, 902–905 (2023).
- Chapin, D. M., Fuller, C. S. & Pearson, G. L. A new silicon pn junction photocell for converting solar radiation into electrical power. *J. Appl. Phys.* **25**, 676 (1954).
- Prince, M. B. Silicon solar energy converters. *J. Appl. Phys.* **26**, 534–540 (1955).
- Loferski, J. J. Theoretical considerations governing the choice of the optimum semiconductor for photovoltaic solar energy conversion. *J. Appl. Phys.* **27**, 777–784 (1956).
- Shockley, W. & Queisser, H. J. Detailed balance limit of efficiency of pn junction solar cells. *J. Appl. Phys.* **32**, 510 (1961).
- Green, M. A., Zhao, J., Wang, A., Reece, P. J. & Gal, M. Efficient silicon light-emitting diodes. *Nature* **412**, 805–809 (2001).
- Green, M. A. Limits on the open circuit voltage and efficiency of silicon solar cells imposed by intrinsic Auger processes. *IEEE Trans. Electron Devices* **31**, 671–678 (1984).
- Tiedje, T., Yablonovitch, E., Cody, D. G. & Brooks, B. G. Limiting efficiency of silicon solar cells. *IEEE Trans. Electron Devices* **31**, 711–716 (1984).
- Yablonovitch, E. Statistical ray optics. *J. Opt. Soc. Am.* **A72**, 899–907 (1982).
- Richter, A., Hermle, M. & Glunz, S. W. Reassessment of the limiting efficiency for crystalline silicon solar cells. *IEEE J. Photovolt.* **3**, 1184–1191 (2013).
- Niewelt, T. et al. Reassessment of the intrinsic bulk recombination in crystalline silicon. *Solar Energy Mater. Solar Cells* **235**, 111467 (2022).
- Kerr, M. J., Cuevas, A. & Campbell, P. Limiting efficiency of crystalline silicon solar cells due to Coulomb-enhanced Auger recombination. *Prog. Photovolt: Res. Appl.* **11**, 97–104 (2003).
- Schäfer, S. & Brendel, R. Accurate calculation of the absorptance enhances efficiency limit of crystalline silicon solar cells with Lambertian light trapping. *IEEE J. Photovolt.* **8**, 1156–1158 (2018).
- Li, Y. et al. Flexible silicon solar cells with high power-to-weight ratios. *Nature* **626**, 105–110 (2024).
- Ivanova, S. M. & Gueymard, C. A. Simulation and applications of cumulative anisotropic sky radiance patterns. *Solar Energy* **178**, 278–294 (2019).
- Jacobson, M. Z. & Jadhav, V. World estimates of PV optimal tilt angles and ratios of sunlight incident upon tilted and tracked PV panels relative to horizontal panels. *Solar Energy* **169**, 55–66 (2018).
- Schuster, C. S. The quest for the optimum angular-tilt of terrestrial solar panels or their angle-resolved annual insolation. *Renew. Energy* **152**, 1186–1191 (2020).
- Campbell, P. & Green, M. A. The limiting efficiency of silicon solar cells under concentrated sunlight. *IEEE Trans. Electron Devices* **33**, 234–239 (1986).
- Campbell, P. & Green, M. A. Light trapping properties of pyramidally textured surfaces. *J. Appl. Phys.* **62**, 243–249 (1987).
- Yu, Z. & Fan, S. Angular constraint on light-trapping absorption enhancement in solar cells. *Appl. Phys. Lett.* **98**, 011106 (2011).
- Gueymard, C. A., Myers, D. & Emery, K. Proposed reference irradiance spectra for solar energy systems testing. *Solar Energy* **73**, 443–467 (2002).
- Khan, M. R., Hanna, A., Sun, X. & Alam, M. A. Vertical bifacial solar farms: physics, design, and global optimization. *Appl. Energy* **206**, 240–248 (2017).
- Fischer, M., Woodhouse, M. & Baliozian, P. *International Technology Roadmap for Photovoltaics (ITRPV)*. <https://www.vdma.org/international-technology-roadmap-photovoltaic> (2024).
- Lorenzo, E., Narvarte, L. & Muñoz, J. Tracking and back-tracking. *Prog. Photovolt. Res. Appl.* **19**, 747–753 (2011).
- Afanasyeva, S., Bogdanov, D. & Breyer, C. Relevance of PV with single-axis tracking for energy scenarios. *Solar Energy* **173**, 173–191 (2018).
- Brendel, R. Coupling of light into mechanically textured silicon solar cells: a ray tracing study. *Prog. Photovolt. Res. Appl.* **3**, 25–38 (1995).
- Rau, U., Paetzold, U. W. & Kirchartz, T. Thermodynamics of light management in solar cells. *Phys. Rev. B* **90**, 035211 (2014).
- Nadi, S. A., Bittkau, K., Lentz, F., Ding, K. & Rau, U. Design of deterministic light-trapping structures for thin silicon heterojunction solar cells. *Optics Express* **29**, 7410 (2021).
- Chong, T. K., Wilson, J., Mokkaṭṭi, S. & Catchpole, K. R. Optimal wavelength scale diffraction gratings for light trapping in solar cell. *J. Opt.* **A14**, 024012 (2012).
- Callahan, D. M., Munday, J. N. & Atwater, H. A. Solar cell light trapping beyond the ray optic limit. *Nano Letters* **12**, 214–218 (2012).
- Landis, G. *Cross-Grooved Solar Cell (Patent 4,608,451)* <https://patents.google.com/patent/US3411952A/en> (1986).
- Tobin, S. P., Keavney, C. J., Geoffroy, L. M. & Sanfalcon, M. M. Experimental comparison of light-trapping structures for silicon solar cells. *Proc. 20th IEEE Photovoltaic Specialists Conf.* 545–548 (IEEE, 1988).
- Yu, Z., Raman, A. & Fan, S. Fundamental limit of light trapping in grating structures. *Optics Express* **18**, A366–A380 (2010).
- Bhattacharya, S. & John, S. Beyond 30% conversion efficiency in silicon solar cells: a numerical demonstration. *Sci. Rep.* **9**, 12482 (2019).
- Bhattacharya, S. & John, S. Light-trapping by wave interference in intermediate-thickness silicon solar cells. *Optics Express* **32**, 29795–29816 (2024).
- Krügener, J. et al. Photonic crystals for highly efficient silicon single junction solar cells. *Solar En. Mat. Solar Cells* **233**, 111337 (2021).
- Schenk, A. Finite-temperature full random-phase approximation model of band gap narrowing for silicon device simulation. *J. Appl. Phys.* **84**, 3684–3695 (1998).
- Schenk, A. Finite-temperature full random-phase approximation of bandgap narrowing in quasi-neutral regions: theory including nonparabolicity and application to silicon and InGaAs. *J. Appl. Phys.* **130**, 015703 (2021).
- Green, M. A. *Third Generation Photovoltaics: Advanced Solar Energy Conversion* 1st edn, Vol. 160 (Springer-Verlag, Berlin, 2003).
- Fell, A. et al. Radiative recombination in silicon photovoltaics: modeling the influence of charge carrier densities and photon recycling. *Solar Energy Mater. Solar Cells* **230**, 111198 (2021).

42. Green, M. A. Lambertian light trapping in textured solar cells and light-emitting diodes: analytical solutions. *Prog. Photovolt Res. Appl.* **10**, 235–241 (2002).
43. Rau, U. Reciprocity relation between photovoltaic quantum efficiency and electroluminescent emission of solar cells. *Phys. Rev. B* **76**, 085303 (2007).
44. van Roosbroeck, W. & Shockley, W. Photon-radiative recombination of electrons and holes in germanium. *Phys. Rev.* **94**, 158–1560 (1954).
45. Green, M. A. Improved silicon optical parameters at 25°C, 295K and 300K including temperature coefficients. *Prog. Photovolt. Res. Appl.* **30**, 164–179 (2022).
46. Thelen, A. Multilayer filters with wide transmittance bands. *J. Opt. Soc. Amer.* **53**, 1266–1270 (1963).

## Acknowledgements

The authors acknowledge support from the Australian Government through the Australian Renewable Energy Agency (ARENA). The Australian Government does not accept responsibility for any information or advice contained herein.

## Author contributions

M.A.G. conceived the compatible projection approach, supervised the project and wrote the first draft of the paper. Z.Z. carried out the detailed light-trapping calculations and prepared the associated figures. Both authors analysed the data and prepared the final version of the text.

## Competing interests

The authors declare no competing interests.

## Additional information

**Supplementary information** The online version contains supplementary material available at <https://doi.org/10.1038/s41467-024-55681-1>.

**Correspondence** and requests for materials should be addressed to Martin A. Green.

**Peer review information** *Nature Communications* thanks the anonymous, reviewer(s) for their contribution to the peer review of this work. A peer review file is available.

**Reprints and permissions information** is available at <http://www.nature.com/reprints>

**Publisher's note** Springer Nature remains neutral with regard to jurisdictional claims in published maps and institutional affiliations.

**Open Access** This article is licensed under a Creative Commons Attribution-NonCommercial-NoDerivatives 4.0 International License, which permits any non-commercial use, sharing, distribution and reproduction in any medium or format, as long as you give appropriate credit to the original author(s) and the source, provide a link to the Creative Commons licence, and indicate if you modified the licensed material. You do not have permission under this licence to share adapted material derived from this article or parts of it. The images or other third party material in this article are included in the article's Creative Commons licence, unless indicated otherwise in a credit line to the material. If material is not included in the article's Creative Commons licence and your intended use is not permitted by statutory regulation or exceeds the permitted use, you will need to obtain permission directly from the copyright holder. To view a copy of this licence, visit <http://creativecommons.org/licenses/by-nc-nd/4.0/>.

© The Author(s) 2024